

Comprehensive Approach to Investigate the De-/Lithiation Mechanism of Fe-Doped SnO₂ as Lithium-Ion Anode Material

Jakob Asenbauer, Anna-Lena Wirsching, Marcel Lang, Sylvio Indris, Tobias Eisenmann, Angelo Mullaliu, Adele Birrozzi, Alexander Hoefling, Dorin Geiger, Ute Kaiser, Rolf Schuster,* and Dominic Bresser*

Iron-doped tin oxide (Sn_{0.9}Fe_{0.1}O₂), and specifically carbon-coated Sn_{0.9}Fe_{0.1}O₂ (Sn_{0.9}Fe_{0.1}O₂-C) provides high reversible capacity and a reasonably low de-/lithiation potential owing to the combined conversion and alloying mechanism. The initial (quasi-)amorphization during the first lithiation, however, renders an in-depth understanding of the reaction mechanism challenging. Herein, a comprehensive investigation via a set of highly complementary characterization techniques is reported, including operando X-ray diffraction, ex situ ¹¹⁹Sn and ⁵⁷Fe Mössbauer spectroscopy, ex situ ⁷Li NMR spectroscopy, operando isothermal microcalorimetry (IMC) of Li|Sn_{0.9}Fe_{0.1}O₂-C coin cells, and electrochemical microcalorimetry of single Sn_{0.9}Fe_{0.1}O₂-C electrodes. The combination of these advanced techniques allows for detailed insights into the lithiation and delithiation mechanism and the potential determining processes, despite the (quasi-) amorphous nature of the active material after the initial lithiation.

1. Introduction

Lithium-ion batteries (LIBs) are the electrochemical energy storage technology of choice to power portable electronic devices and increasingly also (hybrid) electric vehicles.^[1,2] Specifically for the latter application, however, further improvement is needed with respect to the energy and power density of LIBs—especially the potential for fast charging remains an unsolved issue.^[3,4] The major limiting factor in this regard is the graphite-based negative electrode owing to the limited lithiation kinetics and the risk of lithium metal plating at high currents and low temperatures.^[5] Besides Li₄Ti₅O₁₂ as high-power, but low-energy alternative,^[6,7] the majority of potential candidates follows either an alloying mechanism (e.g., Si or Sn^[8–10]), a conversion mechanism (e.g., Fe₂O₃ or CoO^[11–13]), or a combination of these two mechanisms in one single material, also referred to as conversion-alloying materials (CAMs).^[14] A family of CAMs that shows potentially high specific capacities of more than 1000 mAh g⁻¹ and a reasonably low de-/lithiation potential is based on SnO₂. Pure SnO₂, however, suffers from an essentially irreversible conversion reaction, which limits its theoretically available reversible capacity to about 782 mAh g⁻¹, i.e., the theoretical capacity of the alloying reaction. The electrochemical performance of SnO₂-based materials can be improved, for instance, by designing materials with a high amount of oxygen vacancies,^[15] or the utilization of SnO_{2-x}/Fe₂O₃ heteronanocrystals.^[16] Another strategy is, to dope tin oxide with a small amount (e.g., 10%) of a transition metal (TM), with Sn_{0.9}Fe_{0.1}O₂ being presumably the most investigated compound of this kind.^[17–21] The presence of the TM dopant leads to the formation of much smaller Sn⁰ nanograins during the conversion reaction, which is important for the reversibility of the conversion, as it allows for the formation of a percolating conductive network. Further improvement of the cycling stability can be achieved by applying a carbonaceous coating, which raises the electronic conductivity, prevents particle agglomeration, and stabilizes the solid electrolyte interphase (SEI).^[21,22] Although significant knowledge on the structural changes during cycling on the performance of Sn_{0.9}Fe_{0.1}O₂-C has been obtained, a detailed understanding of the reaction mechanism is, however, still missing. Investigations, were limited so far to the application of electrochemical methods and operando X-ray diffraction (XRD) experiments.^[21]

didates follows either an alloying mechanism (e.g., Si or Sn^[8–10]), a conversion mechanism (e.g., Fe₂O₃ or CoO^[11–13]), or a combination of these two mechanisms in one single material, also referred to as conversion-alloying materials (CAMs).^[14] A family of CAMs that shows potentially high specific capacities of more than 1000 mAh g⁻¹ and a reasonably low de-/lithiation potential is based on SnO₂. Pure SnO₂, however, suffers from an essentially irreversible conversion reaction, which limits its theoretically available reversible capacity to about 782 mAh g⁻¹, i.e., the theoretical capacity of the alloying reaction. The electrochemical performance of SnO₂-based materials can be improved, for instance, by designing materials with a high amount of oxygen vacancies,^[15] or the utilization of SnO_{2-x}/Fe₂O₃ heteronanocrystals.^[16] Another strategy is, to dope tin oxide with a small amount (e.g., 10%) of a transition metal (TM), with Sn_{0.9}Fe_{0.1}O₂ being presumably the most investigated compound of this kind.^[17–21] The presence of the TM dopant leads to the formation of much smaller Sn⁰ nanograins during the conversion reaction, which is important for the reversibility of the conversion, as it allows for the formation of a percolating conductive network. Further improvement of the cycling stability can be achieved by applying a carbonaceous coating, which raises the electronic conductivity, prevents particle agglomeration, and stabilizes the solid electrolyte interphase (SEI).^[21,22] Although significant knowledge on the structural changes during cycling on the performance of Sn_{0.9}Fe_{0.1}O₂-C has been obtained, a detailed understanding of the reaction mechanism is, however, still missing. Investigations, were limited so far to the application of electrochemical methods and operando X-ray diffraction (XRD) experiments.^[21]


J. Asenbauer, A.-L. Wirsching, S. Indris, T. Eisenmann, A. Mullaliu, A. Birrozzi, A. Hoefling, D. Bresser
 Helmholtz Institute Ulm (HIU)
 89081 Ulm, Germany
 E-mail: dominic.bresser@kit.edu

J. Asenbauer, A.-L. Wirsching, T. Eisenmann, A. Mullaliu, A. Birrozzi, A. Hoefling, D. Bresser
 Karlsruhe Institute of Technology (KIT)
 76021 Karlsruhe, Germany

M. Lang, R. Schuster
 Institute of Physical Chemistry
 Karlsruhe Institute of Technology (KIT)
 76131 Karlsruhe, Germany
 E-mail: rolf.schuster@kit.edu

S. Indris
 Institute for Applied Materials (IAM)
 Karlsruhe Institute of Technology (KIT)
 76344 Eggenstein-Leopoldshafen, Germany

D. Geiger, U. Kaiser
 Central Facility for Electron Microscopy
 Ulm University
 89081 Ulm, Germany

 The ORCID identification number(s) for the author(s) of this article can be found under <https://doi.org/10.1002/adsu.202200102>.

© 2022 The Authors. Advanced Sustainable Systems published by Wiley-VCH GmbH. This is an open access article under the terms of the Creative Commons Attribution-NonCommercial License, which permits use, distribution and reproduction in any medium, provided the original work is properly cited and is not used for commercial purposes.

DOI: 10.1002/adsu.202200102

Specifically, the latter technique is limited in providing in-depth insights due to the (quasi)amorphous or nanocrystalline nature of the reaction products in the fully lithiated state. In addition, the initial crystalline (or any well-crystallized) structure is not recovered upon delithiation. Nonetheless, the fundamental understanding of the reaction mechanism, also upon delithiation, is of utmost importance to overcome the remaining challenges such as the improvement of the Coulombic efficiency and the reduction of the pronounced voltage hysteresis at elevated potentials.^[23]

Herein, we report the comprehensive investigation of the reaction mechanism by combining highly complementary characterization techniques, including a set of in/ex situ spectroscopic techniques, namely ⁵⁷Fe Mössbauer, ¹¹⁹Sn Mössbauer, ⁷Li magic angle spinning (MAS) nuclear magnetic resonance (NMR), and X-ray absorption spectroscopy (XAS), coupled with operando XRD and operando isothermal microcalorimetry (IMC) of Li||Sn_{0.9}Fe_{0.1}O₂-C coin cells as well as of single Sn_{0.9}Fe_{0.1}O₂-C electrodes. Especially the calorimetric techniques may provide fundamental insights into the parasitic side reactions with the electrolyte and polarization effects, i.e., the origin of the Coulombic inefficiency and (part of) the voltage hysteresis, by following the irreversible and reversible heat evolution during discharge and charge.

2. Results and Discussion

2.1. Physicochemical Characterization of (Fe-doped) SnO₂

The XRD patterns of the three active materials SnO₂, Sn_{0.9}Fe_{0.1}O₂, and Sn_{0.9}Fe_{0.1}O₂-C are presented in **Figure 1a**. The comparison of the XRD patterns with the powder diffraction file (PDF) reference reveals that the reflections are matching well with the reference for tetragonal cassiterite-structured SnO₂ (space group: *P4₂/mnm* with the lattice parameters *a* = 4.737 Å and *c* = 3.185 Å^[24,25]) and no additional reflections were observed, indicating that all materials were phase-pure, that the iron dopant was successfully introduced into the tin oxide lattice, and that the carbon coating did not have an impact on the crystal structure, in line with previous studies.^[20,21] All three diffraction patterns show rather broad reflections, pointing at a small crystallite (and potentially particle) size and/or a low crystallinity. By using the Scherrer equation, an average crystallite size of about 10 nm was calculated for pure SnO₂. For Sn_{0.9}Fe_{0.1}O₂, this value is slightly reduced to around 6 nm, suggesting that the iron doping results in a slightly reduced crystallite size and/or a slightly lower crystallinity. The same crystallite size was obtained for Sn_{0.9}Fe_{0.1}O₂-C, showing that the thermal treatment during the carbon coating does not lead to the sintering of the particles. The morphology

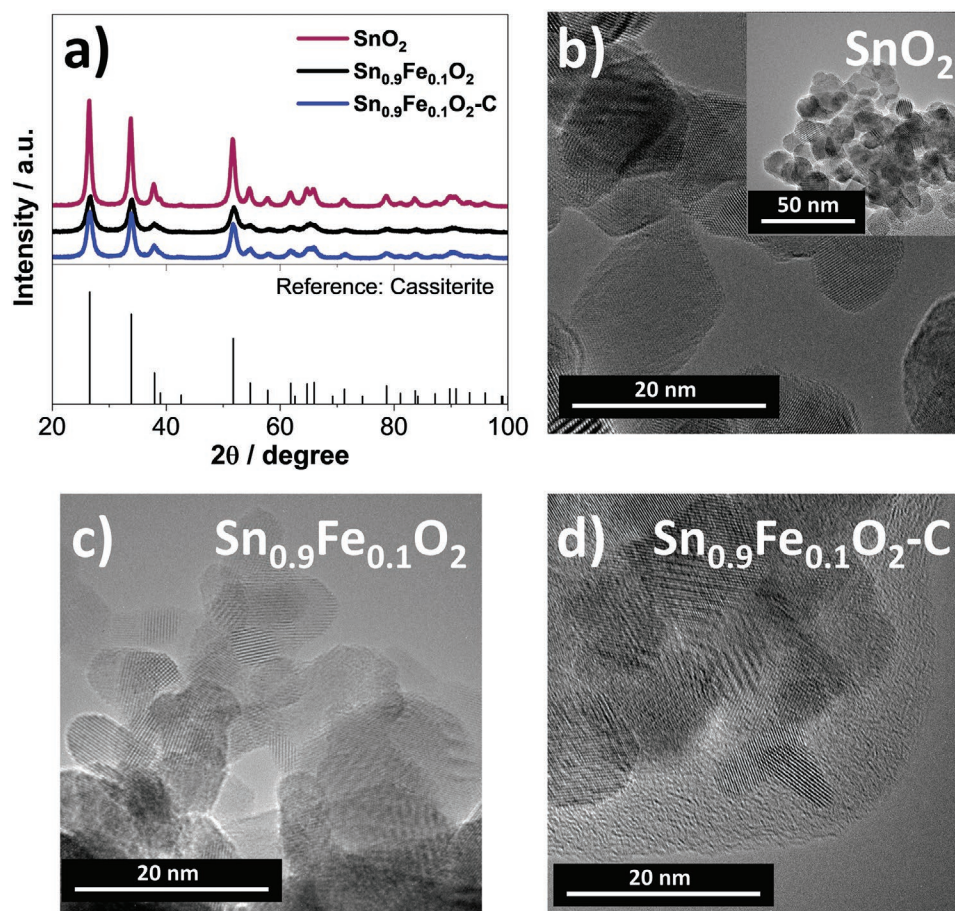


Figure 1. a) X-ray diffraction (XRD) patterns of SnO₂ (in purple), Sn_{0.9}Fe_{0.1}O₂ (in black), and Sn_{0.9}Fe_{0.1}O₂-C (in blue); in the bottom the powder diffraction file (PDF) reference for tetragonal cassiterite-structured SnO₂ (PDF 00-005-0467) is provided. b–d) High-resolution transmission electron microscopy (HRTEM) images of b) SnO₂ (with an image at lower magnification as inset), c) Sn_{0.9}Fe_{0.1}O₂, and d) Sn_{0.9}Fe_{0.1}O₂-C.

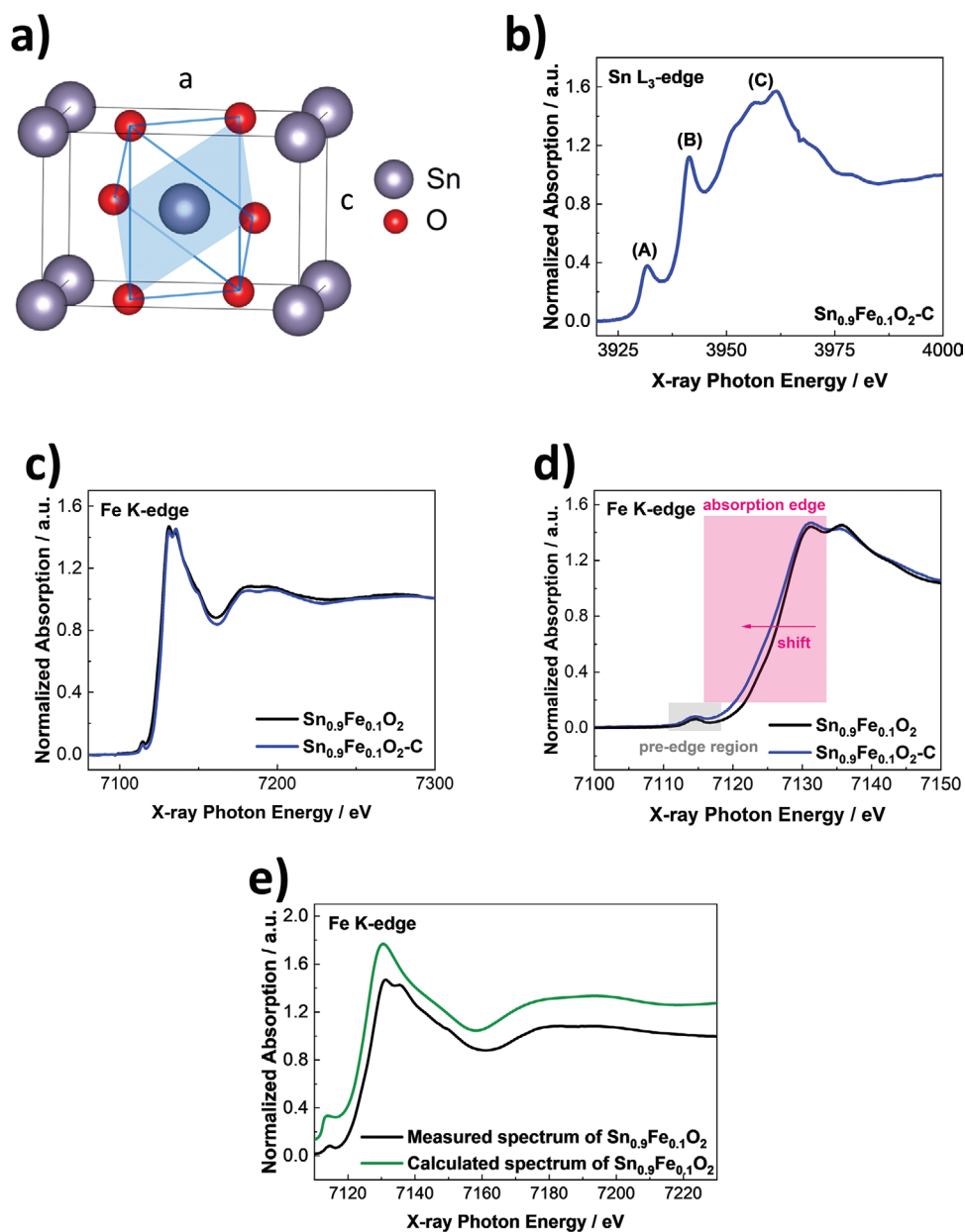


Figure 2. a) Schematic illustration of the SnO_2 cassiterite structure, with tin (gray spheres) being octahedrally coordinated by oxygen (red spheres; lattice parameters: $a = 4.737 \text{ \AA}$ and $c = 3.186 \text{ \AA}$; modified from ref. [24]). b) X-ray absorption near edge structure (XANES) spectrum of $\text{Sn}_{0.9}\text{Fe}_{0.1}\text{O}_2\text{-C}$ at the Sn L_3 -edge. c) XANES spectra of $\text{Sn}_{0.9}\text{Fe}_{0.1}\text{O}_2$ (in black) and $\text{Sn}_{0.9}\text{Fe}_{0.1}\text{O}_2\text{-C}$ (in blue) at the Fe K-edge. d) Close-up of the absorption edge of the two XANES spectra shown in (c). e) Ab initio calculated XANES spectrum for the Fe K-edge of $\text{Sn}_{0.9}\text{Fe}_{0.1}\text{O}_2$ in comparison with the measured XANES spectrum of $\text{Sn}_{0.9}\text{Fe}_{0.1}\text{O}_2$.

and crystallinity of the active materials were analyzed via high-resolution transmission electron microscopy (HRTEM). The HRTEM images of pure SnO_2 , $\text{Sn}_{0.9}\text{Fe}_{0.1}\text{O}_2$, and $\text{Sn}_{0.9}\text{Fe}_{0.1}\text{O}_2\text{-C}$ are displayed in Figure 1b–d, respectively. All three materials are characterized by a very small particle size in the range from 10 to 20 nm, with a trend to slightly smaller particles in the case of $\text{Sn}_{0.9}\text{Fe}_{0.1}\text{O}_2\text{-C}$ (Figure 1c,d) in agreement with the XRD data. In fact, all particles are single-crystalline, i.e., the crystallite size determined by XRD is equal to the average particle size. For $\text{Sn}_{0.9}\text{Fe}_{0.1}\text{O}_2\text{-C}$ (Figure 1d), the primary particle agglomerates are covered by an amorphous carbon layer with a thickness of about

5–10 nm in agreement with a previous study.^[21] Furthermore, TEM EDX mapping of $\text{Sn}_{0.9}\text{Fe}_{0.1}\text{O}_2\text{-C}$ (Figure S1, Supporting Information) shows a homogeneous dispersion of Fe in the sample, along with Sn.

In order to further investigate the impact of the Fe doping on the electronic and local structure, XAS was performed at the Sn L_3 -edge and Fe K-edge. As illustrated in Figure 2a, pure SnO_2 shows a tetragonal cassiterite structure, with six oxygen atoms (represented by the red spheres) octahedrally coordinating each tin (represented by the grey spheres).^[24] The X-ray absorption near-edge structure (XANES) spectrum at the Sn

L_{3} -edge of $\text{Sn}_{0.9}\text{Fe}_{0.1}\text{O}_2\text{-C}$ is presented in Figure 2b and is in good agreement with the spectrum reported for commercial SnO_2 .^[26] According to this earlier study on SnO_2 , the indicated peaks (A), (B), and (C) in the near-edge region of the X-ray absorption edge can be assigned to certain electron transitions to empty or quasi-bound states. Metallic tin has the electron configuration $[\text{Kr}]4d^{10}5s^25p^2$, while Sn^{4+} in SnO_2 shows the electron configuration $[\text{Kr}]4d^{10}$. As a consequence, the 5s orbital is empty and can accommodate electrons, and the transitions (A) and (B) are assigned to the transition from $2p_{3/2} \rightarrow 5s_{1/2}$,^[26] although it would commonly be expected that this transition results in only one peak. However, Fracchia et al.^[26] for instance, ascribed the appearance of two peaks to the covalent character of the Sn–O bond in SnO_2 . This means that the Sn 5s and 5p states are showing some degree of hybridization with the O 2p states from the ligands, which leads to an additional electronic configuration, likely leading to the second peak (B). Most important, though, for the present study is the finding that the tin in $\text{Sn}_{0.9}\text{Fe}_{0.1}\text{O}_2\text{-C}$ has the same oxidation state, lattice position, and coordination as in SnO_2 . To get comparable information about the iron (in the absence and presence of the carbon coating), XANES spectra of both $\text{Sn}_{0.9}\text{Fe}_{0.1}\text{O}_2$ and $\text{Sn}_{0.9}\text{Fe}_{0.1}\text{O}_2\text{-C}$ were recorded at the Fe K-edge (Figure 2c). Overall the two spectra reveal very similar features and both pre-edge features and the main edge positions are qualitatively in line with octahedrally coordinated Fe^{3+} ,^[27] which is in line with an earlier study by X-ray photoelectron spectroscopy (XPS) on noncoated $\text{Sn}_{0.9}\text{Fe}_{0.1}\text{O}_2$.^[21] When having a closer look at the Fe K-edge in the XANES spectra (Figure 2d), though, it is observed that the absorption edge of $\text{Sn}_{0.9}\text{Fe}_{0.1}\text{O}_2\text{-C}$ is slightly shifted toward lower X-ray photon energies. This indicates that iron is partially reduced to a slightly lower oxidation state during the carbon coating process, as also found for Fe-doped ZnO ^[28] and Mn-doped ZnO .^[29] In both cases, however, the experimentally recorded spectra qualitatively match the ab initio calculated XANES spectrum of $\text{Sn}_{0.9}\text{Fe}_{0.1}\text{O}_2$ (Figure 2e), indicating that iron is octahedrally coordinated by six oxygen as the Sn site in SnO_2 , and that the coordination environment is asymmetric.

We may note at this point that the introduction of aliovalent iron into the tin oxide structure is presumably accompanied by the formation of oxygen vacancies and/or interstitial cationic sites. As we cannot safely exclude one or the other, neither quantify the amount of oxygen vacancies, we may continue referring to this material as $\text{Sn}_{0.9}\text{Fe}_{0.1}\text{O}_2\text{-C}$ in the following.

2.2. Investigation of the Reaction Mechanism

For the investigation of the reaction mechanism of $\text{Sn}_{0.9}\text{Fe}_{0.1}\text{O}_2\text{-C}$, we firstly conducted an operando XRD experiment. The results are displayed in Figure S2 (Supporting Information) and are discussed in detail in the Supporting Information. The findings are well in line with a previous operando XRD investigation on $\text{Sn}_{0.9}\text{Fe}_{0.1}\text{O}_2$ ^[21] and generally confirm an initial Li^+ insertion, followed by the reduction of the oxide to metallic tin upon further lithiation and eventually the formation of the Li_xSn alloy. Nevertheless, owing to the (quasi-)amorphous nature of the compounds formed in the discharged (i.e., lithiated) state and the fact that the material remains (quasi-)amorphous also upon delithiation, little information can be

gained beyond the initial lithiation and the iron dopant is essentially invisible in the XRD patterns.

Therefore, we combined the operando XRD analysis with ex situ ^{119}Sn and ^{57}Fe Mössbauer spectroscopy. In addition to the pristine $\text{Sn}_{0.9}\text{Fe}_{0.1}\text{O}_2\text{-C}$ also partially (0.7 V) and fully lithiated (0.01 V) as well as fully delithiated (3.0 V) electrodes were studied. These three different voltage points are highlighted in the cyclic voltammogram in Figure S3 (Supporting Information). The corresponding ^{119}Sn and ^{57}Fe spectra are presented in Figure 3a,b, respectively, and the summaries of the fitting results are provided in Table S1, Supporting Information (^{119}Sn) and Table S2, Supporting Information (^{57}Fe). For the pristine sample, the ^{119}Sn spectrum (Figure 3a) was fitted by a doublet with an isomer shift (IS) of 0.01 mm s^{-1} and a small quadrupole splitting (QS) of 0.41 mm s^{-1} , and thus strongly overlapping lines. These values are characteristic of Sn^{4+} in the cassiterite (SnO_2) structure.^[30] The QS is caused by the intrinsic asymmetry of the SnO_6 octahedra. The partial lithiation to a cut-off voltage of 0.7 V (i.e., below the initial voltage plateau, see Figure S2a, Supporting Information) leads to a decrease of the singlet component of cassiterite tin oxide, accompanied by a slight change of the IS to 0.060 mm s^{-1} . According to the in situ ^{119}Sn Mössbauer investigation by Sandu et al.^[31] such a shift indicates the reinforcement of the SnO_2 lattice as a result of the initial Li^+ insertion, leading to the formation of new Li–O bonds without the destruction of the initial Sn–O bonds. The additionally observed doublet component centered at 1.344 mm s^{-1} is assigned to the presence of metallic tin,^[32] corroborating the assignment of the voltage plateau at $\approx 1.0 \text{ V}$ to the reduction of Sn^{4+} to Sn^0 . In fact, Sandu et al.,^[31] reported that the insertion and further reduction to metallic tin partially overlap, in agreement with the operando XRD data (Figure S2d, Supporting Information). Upon further lithiation to 0.01 V, the ^{119}Sn spectrum reveals an additional peak at 1.127 mm s^{-1} , which has been assigned to metallic tin with metallic bonds to tin and lithium, while there is also still some interaction with oxygen.^[32] Given the absence of any SnO_2 -related reflection in the corresponding XRD data (Figure S2e, Supporting Information), we may assume that this is related to the interaction of the tin (alloy) surface with the surrounding Li_2O matrix and/or the reaction with oxygen traces during the ex situ sample preparation owing to the high reactivity of the fully discharged material. Most interestingly, though, with regard to the (quasi-)amorphous nature of the active material in the delithiated state, is the finding that tin is not fully re-oxidized at 3.0 V. The ^{119}Sn spectrum is comparable to the spectrum recorded for the sample discharged to 0.7 V, indicating that only the alloying reaction is completely reversible, while the conversion reaction, i.e., the re-oxidation to tin oxide remains incomplete. Besides, both components, the one for oxidized tin centered at 0.132 mm s^{-1} and the one for metallic tin centered at 1.599 mm s^{-1} , show increased QS values of 0.463 and 1.244 mm s^{-1} , respectively, as a consequence of the pronounced disorder of the local environment.

For the fitting of the ^{57}Fe Mössbauer spectrum of pristine $\text{Sn}_{0.9}\text{Fe}_{0.1}\text{O}_2\text{-C}$ (Figure 3b), two doublets were necessary to achieve a reasonable fit. This indicates two different Fe environments in the sample, either in one compound or in different phases. The main doublet (86%) with IS = 0.39 mm s^{-1} and QS = 0.87 mm s^{-1} is assigned to Fe^{3+} in the octahedral positions of SnO_2 ,^[33,34] which

is in good agreement with the XAS results and the partial substitution of Sn^{4+} by Fe^{3+} . The second doublet with $\text{IS} = 0.083 \text{ mm s}^{-1}$ and a rather small QS of 0.321 mm s^{-1} indicates the presence of Fe with a different oxidation state, which is in agreement with the XAS results that showed that Fe is partially reduced during the carbon coating process. Two possible explanations for the IS close to 0 mm s^{-1} are possible: (i) this component belongs to Fe^{2+} in a low-spin configuration, or (ii) this component represents Fe^0 inside very small Fe metal clusters that are too small to be detected by XRD and to establish magnetic ordering, while even very minor traces can give a significant signal in the Mössbauer spectra. The HRTEM analysis presented herein (Figure 1d) and in previous studies,^[20,21] however, revealed perfectly crystalline particles also after the carbon coating, suggesting that the signal observed is related to the formation of Fe^{2+} in a low-spin state rather than a complete reduction to the metallic state. The evolution of the ^{57}Fe spectra upon discharge (lithiation) shows that the doublet attributed to Fe^{3+} is gradually shifting from 0.390 mm s^{-1} (pristine state) to 0.346 mm s^{-1} (0.7 V) and further to 0.183 mm s^{-1} (0.01 V). This significant shift indicates a gradual reduction.^[35] Notably, an IS of 0.0 mm s^{-1} , which would correspond to the α -Fe reference, was not reached, neither was the typical hyperfine splitting observed. Given that a preliminary analysis of ex situ XAS data revealed the reduction of the transition metal dopant to the metallic state (not shown herein), a possible explanation for the findings obtained by ^{57}Fe Mössbauer spectroscopy might be the formation of iron metal nanodomains with a superparamagnetic rather than ferromagnetic behavior or the formation of an iron-tin alloy, which would also lead to superparamagnetic behavior.^[35] In fact, an in-depth investigation of iron-doped zinc oxide revealed the formation of an iron-zinc alloy upon lithiation^[36] and it appears likely that such reaction occurs also for iron-doped tin oxide. The subsequent delithiation to 3.0 V reveals a

Fe^{3+} component centered at 0.312 mm s^{-1} , indicating the re-oxidation to Fe^{3+} . This re-oxidation, however, remains incomplete, as apparent from the additionally observed doublet at 0.941 mm s^{-1} with a significantly higher QS of 1.784 mm s^{-1} , which is assigned to the accommodation of Fe^{2+} in an octahedral position.^[33] In fact, an incomplete re-oxidation of the iron dopant was observed also for iron-doped zinc oxide,^[37] suggesting that the two active materials behave similarly upon electrochemical de-/lithiation.

To gain further insights into the reaction mechanism, also ex situ ^7Li MAS NMR spectroscopy was conducted at the same states of dis-/charge (Figure 3c). For the pristine $\text{Sn}_{0.9}\text{Fe}_{0.1}\text{O}_2\text{-C}$, no lithium is found, as expected. In the spectrum recorded for the partially lithiated material (0.7 V), a peak at 0 ppm appears. This peak is assigned to lithium in a diamagnetic environment, i.e., Li_2O ,^[36,38] which is formed along with the formation of metallic tin. Upon further lithiation to 0.01 V the peak intensity is increasing as a result of the ongoing reduction of the initial oxide. These results are in good agreement with the findings obtained by ex situ Mössbauer spectroscopy. In addition, a broad shoulder is observed in the fully lithiated state at 0.01 V, revealing the presence of a second lithium-containing compound, presumably the lithium-tin alloy.^[38] During the subsequent delithiation, this broad shoulder vanishes, confirming the complete reversibility of the alloying reaction, but the peak related to Li_2O remains. While the presence of Li_2O also in the fully delithiated state might in part originate from the formation of the SEI,^[39] the pronounced intensity suggests that the conversion reaction is incomplete, in agreement with the ex situ Mössbauer spectroscopy investigation.

In sum, the ex situ Mössbauer and ^7Li NMR spectroscopy analysis reveals the following findings: (i) In the pristine state, Fe^{3+} is located in the octahedral position of the cassiterite crystal structure, partially replacing tin. (ii) The alloying reaction is

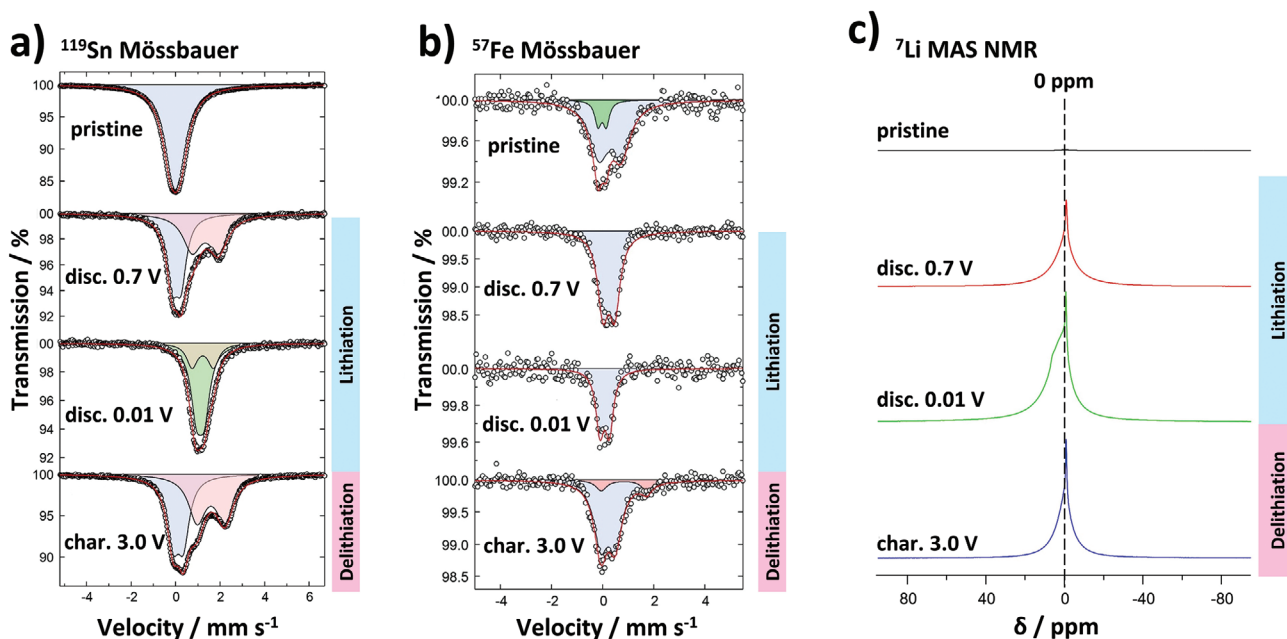


Figure 3. a) ^{119}Sn Mössbauer spectra, b) ^{57}Fe Mössbauer spectra, and c) ^7Li MAS NMR spectra of the pristine $\text{Sn}_{0.9}\text{Fe}_{0.1}\text{O}_2\text{-C}$ and $\text{Sn}_{0.9}\text{Fe}_{0.1}\text{O}_2\text{-C}$ discharged (disc.) and charged (char.) to different states of de-/lithiation, i.e., 0.7 and 0.01 V upon discharge and 3.0 V upon charge.

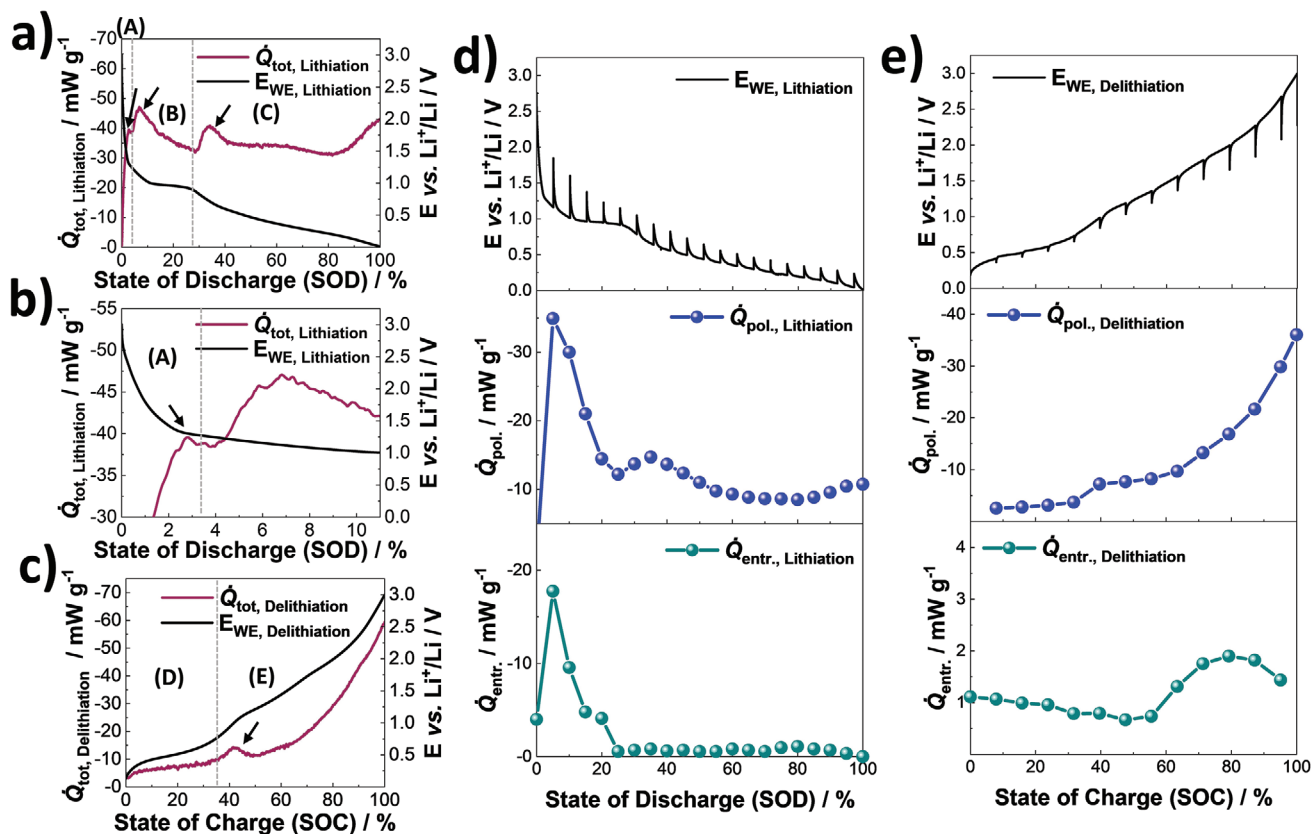


Figure 4. a–c) Normalized heat flow (per mass of the active material; in purple) and the corresponding voltage profile (in black) recorded for a Li||Sn_{0.9}Fe_{0.1}O₂-C coin cell during the operando isothermal microcalorimetry (IMC) experiment with a constant current of 50 mA g⁻¹ ($T = 20\text{ }^{\circ}\text{C}$; the lower cut-off voltage was set to 0.01 V and the upper one to 3.0 V): a) The evolution of the normalized heat flow and voltage during discharge; b) magnification of the initial part of the discharge process; c) the evolution of the normalized heat flow and voltage upon charge. d,e) Results of the galvanostatic intermittent titration technique (GITT) experiment for the d) lithiation and e) delithiation of Sn_{0.9}Fe_{0.1}O₂-C in a coin cell (specific current: 50 mA g⁻¹) with the voltage profile of the GITT experiment (top, in black), the estimated polarization heat flow \dot{Q}_{pol} (middle, in blue), and the entropic heat flow \dot{Q}_{entr} (bottom, in turquoise).

fully reversible, while the conversion reaction and re-oxidation of tin and iron remain incomplete.

To complement the operando XRD and ex situ Mössbauer spectroscopy and ⁷Li MAS NMR study, operando IMC was performed in order to gain additional insights into the de-/lithiation mechanism. The recorded heat flow and the corresponding voltage profile of the Li||Sn_{0.9}Fe_{0.1}O₂-C cell are presented in Figure S4 (Supporting Information). A more detailed analysis following a normalization of the recorded heat flow to the mass of the Sn_{0.9}Fe_{0.1}O₂-C active material is presented in Figure 4a–c. The initial discharge is displayed in Figure 4a. Generally, the heat flow profile reveals three distinct peaks at 3% (see Figure 4b for a magnification of the first part of the discharge), 7%, and 34% state of discharge (SOD), which is in accordance with the inflection points of the corresponding voltage profile. Additionally, an increase in heat flux is observed starting from about 80% SOD. Following the three distinct peaks, the heat flow, and voltage profile are separated into three regions, i.e., Region (A)–(C). The first peak in Region (A) at 3% SOD is assigned to the initial insertion of lithium into the cassiterite host structure,^[31] in accordance with the previous findings. The second peak at 7% SOD appears just ahead of the

voltage plateau at around 1.0 V. Hence, the peak in the heat profile is attributed to the nucleation of the second phase, i.e., metallic tin and Li₂O, which is formed along the voltage plateau.^[36] Finally, Region (C) is attributed to the formation of the lithium-tin alloy (along with a further reduction of the oxide to metallic tin, as observed from the previous experiments) and the eventual increase in heat flow starting from about 80% SOD is assigned to the decomposition of the electrolyte.

During the subsequent delithiation (Figure 4c) the heat flow is generally much lower, which very well reflects the voltage hysteresis. Besides, the delithiation heat flow reveals an essentially continuous increase, though with a varying slope, and is roughly divided into two regions, i.e., Region (D) and Region (E), according to the peak observed for the heat flow and the inflection point of the voltage profile that occur at the same state of charge (SOC). In Region (D), the heat flow increases only very slowly up to about 35% SOC. The corresponding part of the voltage profile has been assigned to the dealloying reaction, which appears to be a kinetically favorable process. The subsequent Region (E) commences with a peak at about 42% SOC along with the inflection point of the charge profile. Hence, this peak is attributed to the onset of the reconversion

of metallic tin and iron to the corresponding oxides. The further course of the graph shows a steep increase in heat flow, finally reaching around -59 mW g^{-1} at the cut-off voltage of 3.0 V. In other words, the reconversion reaction is characterized by a substantially larger heat flow than the dealloying reaction.

Generally, the total heat flux caused by the electrochemical dis-/charge process consists of three contributions: (i) a reversible contribution \dot{Q}_{entr} , that reflects the entropy change during the electrochemical processes, which changes its sign when the direction of the electrochemical processes, i.e., the current direction is inverted; (ii) an irreversible contribution \dot{Q}_{pol} , which always leads to the evolution of heat owing to the deviation from equilibrium during current flow; and (iii) the Joule heat that is caused by the current flow through the electrolyte and which also always produces heat. For a further evaluation of these different contributions to the overall heat flow, the galvanostatic intermittent titration technique (GITT), including a variation of the temperature during the open circuit voltage (OCV) step, was used. During the intermittence of the dis-/charge process, the cell voltage relaxed from the cell voltage with current flow E_{load} to the (close-to) equilibrium open cell voltage E_{OCV} . For the determination of the irreversible, polarization-related heat flow \dot{Q}_{pol} , E_{load} and E_{OCV} were estimated from the voltage profiles during intermittent discharging and charging shown in the upper panels of Figure 4d,e. Note that only the sections with current flow are depicted. During the discharge process in Figure 4d the cell voltage drops to its value for steady current flow E_{load} , while during the intermittence periods (not shown) the cell voltage relaxes positive toward E_{OCV} . The difference $E_{\text{load}} - E_{\text{OCV}}$ corresponds to the overpotential, i.e., the deviation from equilibrium. Multiplying the overpotential with the applied specific current of 50 mA g^{-1} yields the corresponding irreversible heat flux \dot{Q}_{pol} . The entropic heat flow contribution \dot{Q}_{entr} corresponds to the reversible heat flow and was derived by measuring the change of the OCV upon temperature steps of $\Delta T = 10 \text{ K}$, that is the temperature coefficient of the cell potential, which is proportional to the reaction entropy of the cell reaction. The Joule heat is estimated from the electrolyte resistance ($\approx 8 \Omega$) and amounts to about 0.03 mW g^{-1} , which is much smaller than the other two contributions and which is therefore neglected in the following discussion. The corresponding values of \dot{Q}_{pol} and \dot{Q}_{entr} for the de-/lithiation of the $\text{Li}|\text{Sn}_{0.9}\text{Fe}_{0.1}\text{O}_2\text{-C}$ coin cells are presented in Figure 4d along with the GITT experiment. The polarization heat flow \dot{Q}_{pol} reveals an initial rapid decrease after a jump from the first to the second data point, followed by a small local maximum at about 35% SOD. The latter is in accordance with the second peak in Figure 4a that has been assigned to the onset of the alloying reaction. Similarly, the entropic heat flow \dot{Q}_{entr} shows a distinct peak at $\approx 5\%$ SOD, which is in line with the second peak at 7% SOD in Region (B) of the IMC experiment, given the resolution of the experiment. This large increase in \dot{Q}_{entr} with a minimum of -18 mW g^{-1} is attributed to the onset of the conversion reaction, i.e., the reduction of the oxide to the metals and the decay of the crystalline structure. Note that the entropic heat flux \dot{Q}_{entr} reflects the entropy change of the cell reaction, including both the lithiation/delithiation of the iron-doped tin oxide and the reaction at the counter electrode, i.e., the Li^+/Li bulk metal deposition/dissolution reaction. The entropic contribution of

the half cell reaction will be explicitly discussed below. Subsequently, at higher SOD, \dot{Q}_{entr} decreases steadily until it reaches a constantly small value of less than 1 mW g^{-1} . In accordance with our earlier study on iron-doped zinc oxide,^[36] it is concluded that overall \dot{Q}_{pol} and specifically \dot{Q}_{entr} show more pronounced variations for the conversion reaction.

Upon delithiation (Figure 4e), \dot{Q}_{pol} is constantly increasing until it reaches 36 mW g^{-1} at the cut-off voltage of 3.0 V. There is a small step-like increase observed at about 40% SOC, which coincides with the peak in the overall heat flow (Figure 4c), indicating the onset of the reconversion reaction. \dot{Q}_{entr} remains generally rather small, never exceeding 2 mW g^{-1} . Nonetheless, there is a significant increase when the reconversion sets in, before it decreases again toward the end of the charge process. It is noteworthy that \dot{Q}_{entr} , determined for the discharge and charge processes, coincides nicely for high Li contents, i.e., for SODs $>40\%$ and SOC $<60\%$, respectively, which signals high reversibility of the lithiation/delithiation process at higher Li contents. However, at lower Li concentrations rather pronounced deviations occur. In particular the rather steep peak of \dot{Q}_{entr} upon lithiation extending from 0% to 20% SOD becomes smeared out between 60% and 100% SOC upon delithiation. This may be attributed, e.g., to SEI formation and irreversible structural transformations, namely the incomplete recovery of the cassiterite structure during the first dis-/charge cycle, as discussed above.

To corroborate the above measurements of the reversible contribution to the heat flux \dot{Q}_{entr} and to obtain information about the timescale on which the reversible processes occur, we performed electrochemical microcalorimetric measurements of the reversible heat/cold evolution at the $\text{Sn}_{0.9}\text{Fe}_{0.1}\text{O}_2\text{-C}$ electrode, i.e., of the half-cell electrode reactions. In the following, this method is abbreviated half-cell microcalorimetry (HCMC).^[40–42] For this purpose, we measured the temperature at the back of a thin $\text{Sn}_{0.9}\text{Fe}_{0.1}\text{O}_2\text{-C}$ electrode with a thin pyroelectric sensor, while the charging or discharging reaction is conducted for 10 ms by a small potential pulse, starting from a well-equilibrated rest potential. Such a 10 ms pulse duration is short enough to avoid heat dissipation into the bulk of the electrolyte and long enough that the electrode-sensor assembly becomes thermally equilibrated.

Figure 5 shows typical potential, current, and temperature transients for the lithiation and delithiation at a rest potential of 0.07 V, corresponding to a SOD of about 90%, which is well in the lithium-tin alloy phase. When the potential pulse is applied, at $t = 10 \text{ ms}$, the current peaks and the temperature at the electrode start to fall for the negative potential pulse (lithiation), while it begins to rise for the positive pulse (delithiation), signaling cold or heat evolution, respectively, caused by the electrochemical electrode processes. At $t = 20 \text{ ms}$ the cell was switched to open cell conditions and the outer current flow ceased. The potential slightly relaxed on a timescale of roughly 100 ms. Shortly after the current ceased, the temperature transients reached a minimum for the delithiation and a maximum for the lithiation process. After reaching its extremum the temperature relaxed toward the temperature before the application of the pulses by dissipation of cold/heat into the electrolyte. From simulations and the pyroelectric coefficients of the sensor we estimate that the overall temperature change is well below 1 mK. Thus our measurements proceeded quasi-isothermal.

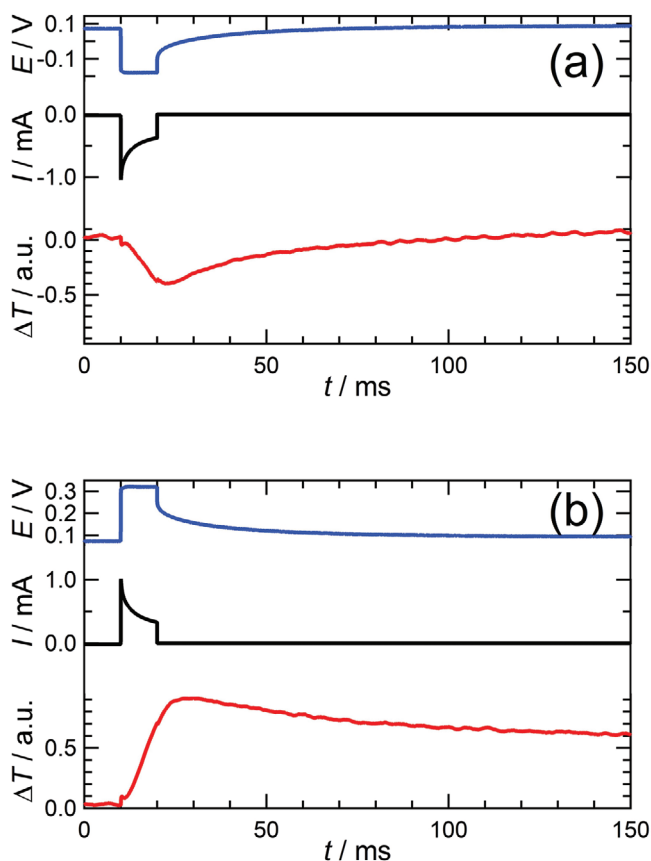


Figure 5. Potential E , current I , and temperature T transients, measured by half-cell microcalorimetry (HCMC) at a single $\text{Sn}_{0.9}\text{Fe}_{0.1}\text{O}_2\text{-C}$ electrode during a) discharge and b) charge with 10 ms potential pulses of ± 100 mV amplitude. The rest potential was 0.072 V, i.e., at 90% state of discharge (SOD) before applying the potential pulses.

The symmetric behavior of the current and temperature transients in Figure 5a,b under potential pulse inversion already signals a high degree of reversibility of the electrochemical dis-/charge processes in the pulse experiments. Note that the electrochemical conversion during each pulse amounted to only ≈ 7 mC g^{-1} in the depicted experiments, which has to be compared with the theoretical capacity of the material (≈ 4300 C g^{-1}) and therefore corresponds to only $\approx 1.6 \times 10^{-4}\%$. A closer inspection of the results reveals that the absolute value of the temperature variation upon cooling is about half of that during warming, although the absolute amount of charge, which flowed during the potential pulses, is about the same for both pulse directions (with a deviation of about 9%). This reflects irreversible contributions to the total heat, which do not change their sign upon current reversal, while the entropic contributions to the heat change their sign. In other words, due to irreversibly exchanged heat, the electrode becomes less cold upon lithiation and warmer upon delithiation than it would be expected for a purely reversible behavior. The irreversible contribution can be directly removed from the temperature transients by subtracting temperature transients obtained from the positive and negative potential pulses. This results in an (averaged) temperature transient, representing the reversible warming or cooling of the electrode during the electrode reaction. By this

procedure also experimental artifacts such as long-term temperature drifts or heat from ongoing background reactions are removed. The closer inspection of the temperature transients in Figure 5 for longer times indeed reveals that the temperature relaxation upon cooling (Figure 5a) is faster than that upon warming (Figure 5b), indicating background heat evolution, probably due to side reactions such as an ongoing SEI formation and electrolyte decomposition. Note that we are extremely sensitive to background processes, since their continuous heat evolution adds to the potential-pulse driven heat evolution of only 10 ms duration. Indeed, ongoing heat evolution due to background processes rendered it impossible to measure the heat during the first discharge step. Only after conditioning the electrode by a slow voltammetrically controlled dis-/charge cycle (1 mV s^{-1} ; $3.0 \text{ V} \rightarrow 0.01 \text{ V} \rightarrow 3.0 \text{ V}$) background heat evolution becomes sufficiently small for the reliable determination of the pulse-driven heat evolution. From the averaged reversible temperature transients, absolute values for the reversible heat exchange were derived (see the Experimental Section for more details on the procedure). To include also reversible heat exchange during the relaxation period, we integrated the reversible heat flux up to 100 ms after the onset of the potential pulse.

Figure 6 depicts the reversible molar heat of the discharge process at the $\text{Sn}_{0.9}\text{Fe}_{0.1}\text{O}_2\text{-C}$ electrode, i.e., for the cathodic process direction (red circles). The right axis gives the corresponding reaction entropy for the discharge process. We plotted the data versus the SOD, as obtained from the voltage profile of the second dis-/charge cycle (Figure S5, Supporting Information). Since the HCMC experiments started at well relaxed rest potentials, this procedure disregards the polarization overpotential, which is included in the voltage profile and may thus lead to an underestimation of the SOD. For the comparison with the GITT experiment, we included the corresponding reversible molar heat for the half-cell reaction at the $\text{Sn}_{0.9}\text{Fe}_{0.1}\text{O}_2\text{-C}$ electrode in Figure 6 (black crosses), as calculated from the entropic heat flux in the lower panel of Figure 4d. For this purpose, the entropic heat flux data were divided by the specific current, yielding the reversible molar heat for the lithiation process in the $\text{Li}||\text{Sn}_{0.9}\text{Fe}_{0.1}\text{O}_2\text{-C}$ coin cell. This had to be offset by the reversible molar heat of the lithium metal deposition at the Li counter electrode, which we determined in a previous work to be 48 kJ mol^{-1} , corresponding to a reaction entropy of $160 \text{ J mol}^{-1} \text{ K}^{-1}$.^[43,44] This value is indicated as a dashed horizontal line in Figure 6. Both datasets, the GITT data from the first discharge and the HCMC data obtained for the second discharge process, nicely coincide. In particular for high SODs $\geq 20\%$, both datasets reach the same high reversible molar heat or reaction entropy for the lithiation process of approximately 48 kJ mol^{-1} or $160 \text{ J mol}^{-1} \text{ K}^{-1}$. At low SOD ($< 20\%$) both measurements exhibit a minimum of only about 15 kJ mol^{-1} ($50 \text{ J mol}^{-1} \text{ K}^{-1}$), whereas at the very beginning of the charge process a steep decrease of the reaction entropy is observed with an increasing SOD.

The differences between both datasets, namely the broader minimum of the HCMC data for SODs $< 20\%$ and the lower molar heat at the very beginning of the discharge process, are not too surprising when considering that the HCMC data were measured during the second dis-/charge cycle, where the original cassiterite structure of the iron-doped tin oxide

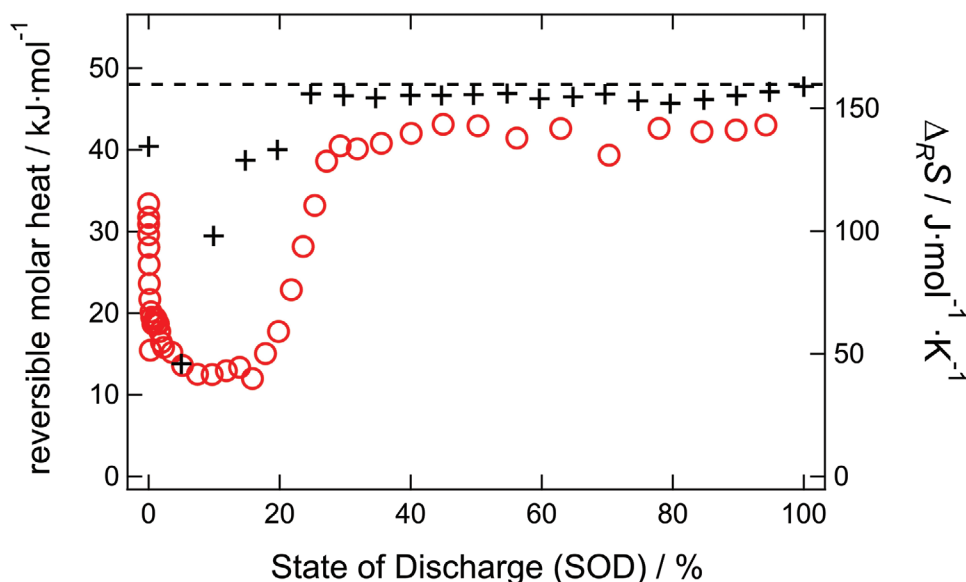


Figure 6. Reversible molar heat (left axis) and reaction entropy of the cathodic (discharge) process (right axis) at a $\text{Li}^+|\text{Sn}_{0.9}\text{Fe}_{0.1}\text{O}_2\text{-C}$ electrode. The red circles mark data points obtained by half-cell microcalorimetry (HCMC) during the second discharging cycle. The corresponding state of discharge (SOD) was determined from the voltage profile in Figure S5 (Supporting Information). In addition, black crosses mark data derived from galvanostatic intermittent titration technique (GITT) experiments during the first discharge.

was considerably degraded and became rather amorphous. These changes are also reflected in the voltage profile, where the pronounced plateau at about 1.0 V in the first cycle became considerably smeared out and shifted to lower voltages in the second cycle (cf. Figure 4a and Figure S5, Supporting Information). In addition, the close resemblance of the GITT and the HCMC data, namely the rather identical spans of the entropy variations, clearly shows that both methods measure the same potential-determining electrochemical processes, albeit the timescale of both measurements is rather different. In the GITT experiment, the system was given 2 h to equilibrate after a temperature step, while for the HCMC measurements the heat or cold evolved mainly during a 10 ms potential step. Thus, the potential-determining reactions, i.e., the electrochemically driven discharge and charge processes are fast, leading to a robust electrochemical equilibrium, which is only negligibly distorted by parasitic processes like phase transitions, electrolyte decomposition, and/or SEI formation.

At high SODs, where the lithium-tin alloy formation is the prevailing process, the reversible molar heat of lithiation comes very close to the molar heat for reversible Li metal deposition (dashed line in Figure 6). The high value of the molar heat for the Li deposition was attributed to the strong solvation of the Li^+ ions in solution.^[43,44] Upon deposition of metallic Li, about 4 to 5 solvent molecules, previously bound in the solvation shell of a Li^+ ion, are set free, leading to a strong increase in entropy, which largely overcompensates the entropy loss due to fixation of Li at the electrode during the deposition process. This latter entropy loss owing to the fixation of Li in the metallic phase was estimated to amount to about $-43 \text{ J mol}^{-1} \text{ K}^{-1}$ (-13 kJ mol^{-1}), whereas the entropy change of the desolvation process amounted to $214 \text{ J mol}^{-1} \text{ K}^{-1}$ (64 kJ mol^{-1}).^[44] Hence, the close match between the lithiation entropy for the lithium-tin alloy with that of lithium metal deposition implies that

the entropy of Li in the alloy phase is close to that of Li metal without pronounced influence of the disorder of the alloy. Indeed, assuming ideal solution behavior, the expected increase of the entropy of Li in the alloy phase upon diluting the Li concentration by a factor of 10 amounts to only $19 \text{ J mol}^{-1} \text{ K}^{-1}$, which would result in a decrease of the reversible molar heat of the lithiation process by only 5.7 kJ mol^{-1} . Therefore, at intermediate to high lithium contents in the lithium-tin alloy no significant variation of the molar heat is expected with a variation of the SOD, and the plateau of the molar heat between $25\% < \text{SOD} < 100\%$ can be well assigned to the desolvation and reduction of Li^+ and subsequent alloying into the lithium-tin alloy phase. Only below $\approx 25\%$ SOD the molar heat steeply decreases by roughly 30 kJ mol^{-1} and reaches a minimum at around 10% SOD. This strong decrease cannot be explained by gradual dilution effects of Li in the metal phase, but rather indicates a change in the discharge process. The low entropy values strongly suggest that there is no significant desolvation of Li^+ ions involved in the electrochemical processes in this SOD range. This is compatible with pure reduction of the iron-doped tin oxide. For very low SODs, the reversible molar heat for the discharging process increases up to 30 kJ mol^{-1} for the HCMC data and even higher for the GITT experiments. Although the definite assignment of a particular reaction mechanism is not possible at this stage, the high reaction entropy at very low SODs is compatible with the desolvation of Li^+ ions and an initial insertion-type reaction prior to the reduction of the oxides to the metallic state.

Following a simplified energy balance model for batteries, which has been developed by Downie et al.,^[45] the parasitic heat flow, e.g., due to irreversible phase transitions of the electrode material, SEI formation, and/or electrolyte decomposition, can be calculated by subtracting $\dot{Q}_{\text{pol.}}$ and $\dot{Q}_{\text{entr.}}$ from the total heat flow. Therefore, $\dot{Q}_{\text{pol.}}$ and $\dot{Q}_{\text{entr.}}$, which were determined by GITT,

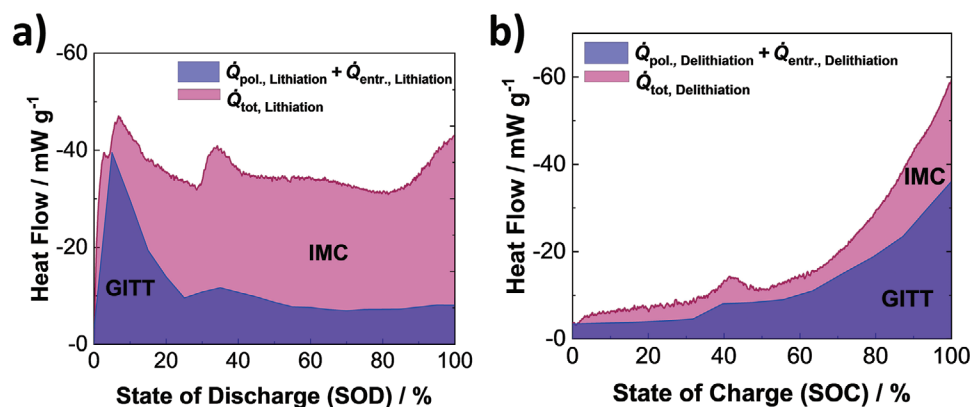


Figure 7. Comparison of the total heat flow measured by operando isothermal microcalorimetry (IMC; in red) and the sum of $\dot{Q}_{\text{pol.}}$ and $\dot{Q}_{\text{entr.}}$ (in blue), as determined by galvanostatic intermittent titration technique (GITT) for the electrochemical a) lithiation and b) delithiation of $\text{Li}||\text{Sn}_{0.9}\text{Fe}_{0.1}\text{O}_2\text{-C}$ in a coin cell (specific current: 50 mA g^{-1} ; cut-off voltages: 0.01 and 3.0 V).

were compared with the overall heat flow measured during the operando IMC experiment (Figure 7). Given the different experimental conditions for the two experiments this comparison is more qualitative than quantitative, but still provides interesting insights into the reaction mechanism. Generally, upon discharge (Figure 7a) the two main peaks for the onset of the conversion and alloying reaction are well apparent from both plots and the overall trend is the same, except beyond an SOD of about 80%, where the IMC-derived heat flow increases, while the GITT-derived heat contributions remain fairly constant. This indicates that at such low potentials, the contribution of the parasitic heat flow becomes increasingly relevant, thus, further corroborating the earlier assignment to reductive electrolyte decomposition. For the delithiation process (Figure 7b), the two profiles generally match each other very well, while the increase in heat flow toward the upper cut-off is more pronounced for the IMC-derived data than for the GITT-derived data, indicating that also the SEI reformation that occurs at such elevated potentials adds to the parasitic heat.^[36,39,46] In combination with the generally higher heat flow for the conversion contribution, these findings provide an explanation for the beneficial impact of lower cut-off voltages on the energy efficiency in lithium-ion cells.^[23]

3. Conclusions

In this work, the de-/lithiation mechanism of $\text{Sn}_{0.9}\text{Fe}_{0.1}\text{O}_2\text{-C}$ was comprehensively investigated by a combination of various complementary operando and ex situ characterization techniques. The findings reveal a three-step lithiation mechanism, including an initial Li^+ insertion, followed by the reduction to the metallic phases and the eventual alloying reaction. These three steps, however, partially overlap—at least under the given experimental conditions. The subsequent delithiation occurs in two steps beginning with the dealloying, followed by the reconversion; the latter, though, remains partially incomplete, while the alloying reaction is fully reversible. This partially incomplete reconversion is accompanied by a significant heat release owing to the reformation of the SEI, highlighting the importance of lower cut-off voltages for such anode materials

when employed in lithium-ion cells, which is also beneficial for achieving a high energy efficiency, i.e., a limited voltage hysteresis, and maintaining a high full-cell voltage also at decreasing SOC. Last but not least, this study highlights the need for a comprehensive approach to investigate the reaction mechanism of new electrode active materials via a set of complementary experimental methods, particularly if such materials are amorphous or turn amorphous during the initial lithiation.

4. Experimental Section

Materials Synthesis: $\text{Sn}_{0.9}\text{Fe}_{0.1}\text{O}_2$ was synthesized in a similar manner as reported earlier.^[20] In brief, 0.482 g (0.001 mol) iron(II) gluconate dihydrate (Alfa Aesar) and 10.262 g (0.030 mol) sucrose (Merck) were dissolved in 100 mL ultrapure water. Upon continuous stirring, 20 mL acetic acid (Sigma Aldrich) and 2.131 g (0.009 mol) tin(II) acetate (Alfa Aesar) were successively added to the solution, which was stirred for another 1.5 h. Subsequently, the solution was heated to 50 °C for 30 min, before evaporating the water at 180 °C for 5 h. The remaining black solid was further dried at 80 °C overnight and then manually ground in an agate mortar prior to the calcination at 450 °C for 3 h (heating rate: $3 \text{ }^\circ\text{C min}^{-1}$) under ambient atmosphere. Pure tin(IV) oxide (SnO_2) was prepared accordingly, but without the addition of iron(II) gluconate dihydrate. For the carbon coating of $\text{Sn}_{0.9}\text{Fe}_{0.1}\text{O}_2$ ($\text{Sn}_{0.9}\text{Fe}_{0.1}\text{O}_2\text{-C}$), 1.200 g (0.007 mol) glucose (VWR Chemicals) was dissolved in 80 mL ultrapure water. Then, 800 mg of $\text{Sn}_{0.9}\text{Fe}_{0.1}\text{O}_2$ was added. The resulting dispersion was transferred into a stainless steel autoclave (Berghof BR-100) and heated to 180 °C under continuous stirring for 13 h. The resulting precipitate was rinsed five times with 30 mL ultrapure water and two times with ethanol in a centrifuge before drying at 80 °C overnight. Finally, the powder was thermally treated at 500 °C for 4 h under an argon atmosphere (heating rate: $3 \text{ }^\circ\text{C min}^{-1}$) to obtain the final product.

Physicochemical Characterization: The crystal structure of the synthesized samples was investigated via XRD using a Bruker D8 Advance diffractometer (Cu-K α radiation, $\lambda = 0.154 \text{ nm}$) within a 2θ range from 20° to 100°. The carbon content in $\text{Sn}_{0.9}\text{Fe}_{0.1}\text{O}_2\text{-C}$ was determined by thermogravimetric analysis (TGA; Model Q5000, TA Instruments) under an oxygen atmosphere in a temperature range from 40 °C to 850 °C with a heating rate of $5 \text{ }^\circ\text{C min}^{-1}$, yielding 13 wt% of carbon. HRTEM was performed on an image Cs-corrected FEI Titan 80–300 kV at 300 kV and STEM-EDX measurements were recorded using a Thermofisher Talos 200X TEM equipped with a SuperX EDX detector at 200 kV. XAS was conducted at the XAFS beamline of the Elettra Synchrotron in Trieste, Italy. The storage ring was operated at

2.0 GeV in top-up mode with a current of 280 mA. The experiments were performed at the Sn L_3 -edge and Fe K-edge in transmission mode by using three ionization chambers filled with appropriate mixtures of argon, nitrogen, and helium optimized to achieve the optimum level of absorption in each chamber. The white beam was monochromatized by using a fixed exit monochromator equipped with a pair of Si(111) crystals. Elemental Sn ($L_3 = 3929$ eV) and Fe ($K = 7112$ eV) reference samples, placed between the second and the third chamber, were used for the energy calibration in each scan, which allowed for continuous monitoring of the energy. The absorption edge energy was determined as the first inflection point of the spectrum. The spectra were processed using the Demeter package. Normalization, background subtraction, energy calibration, and alignment were performed using the Athena software. The ab initio simulation of the XANES spectrum of the Fe K-edge was performed using the FDMNES software.^[47] The Fe K-edge was calculated in the photoelectron energy range $-5 < E < 120$ eV with respect to the Fermi energy level using the Multiple Scattering Theory (MST). The Hedin–Lundqvist complex potential^[48] was used to calculate the excited states, while the absorption cross-section was calculated within the dipolar approximation. A discrete FeO_6 cluster with an asymmetric coordination environment was considered and the best agreement between experiment and calculation was obtained by fixing the Fe–O bond lengths to 2.12 Å (x3), similar to hematite, or contracted to 90% (x3) of that value.

Operando XRD: For the operando XRD measurements, a self-designed two-electrode cell was used.^[49] The slurry, comprising the active material, conductive carbon (Super C65, IMERYS), and the binder (sodium carboxymethyl cellulose; CMC; Dow Wolff Cellulosics) in a weight ratio of 75:20:5, was homogenized using a planetary ball-mill (Pulverisette 4; Fritsch; milling conditions: 4×30 min at 400/–800 rpm with 10 min rest in-between). The resulting dispersion was cast directly on a beryllium disc (25 mm diameter, 0.25 mm thickness; Materion), which served simultaneously as the current collector and “window” for the X-ray beam. The coated Be disc was dried for 4 h at room temperature and 60 °C under vacuum overnight. Metallic lithium (battery grade, Honjo) was used as the counter and reference electrode and two Whatman separators ($\varnothing = 19$ mm) drenched with 300 μL of the electrolyte (1 M LiPF_6 in a 1:1 mixture of ethylene carbonate (EC) and dimethyl carbonate (DMC); UBE) served as the separator. Upon de-/lithiation, the X-ray diffractograms were measured in a 2θ range of $22^\circ \leq 2\theta \leq 50^\circ$.

Ex situ ^7Li NMR and Mössbauer Spectroscopy: For the ex situ ^7Li NMR and Mössbauer spectroscopy investigation, $\text{Sn}_{0.9}\text{Fe}_{0.1}\text{O}_2\text{-C}$ was mixed with the conductive carbon in a ratio of 75:20 and dried overnight at 120 °C under vacuum. The resulting powder was transferred into an argon-filled glovebox (with an oxygen and water content below 0.1 ppm), in which pellets with a diameter of 8 mm and a mass of approximately 35 mg were pressed. These pellets were used as working electrodes in Swagelok-type T-cells with lithium metal foil (battery grade; Honjo) as counter and reference electrodes. A Whatman glass fiber sheet was used as the separator and drenched with 300 μL of the aforementioned electrolyte. The T-cells were cycled to specific cut-off potentials of 0.7 and 0.1 V upon lithiation and 3.0 V upon delithiation using a BioLogic VMP3 potentiostat/galvanostat. Subsequently, the cells were disassembled in the glove box and the pellets were rinsed with 150 μL DMC to remove any residual electrolyte. The Mössbauer spectroscopy measurements were performed in transmission mode at room temperature in a constant acceleration spectrometer. For the ^{119}Sn and ^{57}Fe Mössbauer spectroscopy experiments, a CaSnO_3 and a $^{57}\text{Co}(\text{Rh})$ source were used, respectively. For each measurement, the corresponding powder was sealed in a polyethylene bag under an argon atmosphere to avoid any contact with air and moisture. ^7Li NMR spectroscopy was performed on a Bruker Avance 200 MHz spectrometer with a magnetic field of 4.7 T. Magic-angle spinning was performed in 1.3 mm rotors at 60 kHz. An aqueous 1 M LiCl solution served as a reference for the NMR shift (0 ppm).

Operando Isothermal Microcalorimetry: The determination of the total heat flow under isothermal conditions was conducted with a TAM IV microcalorimeter (TA Instruments), equipped with a custom-made sample holder for coin cells with a Cu-P-bronze wire (36A AWG). For

the coin cell assembly, electrodes were prepared by manually mixing the active material and the conductive carbon, before adding the mixture to a 1.25 wt% solution of CMC in ultrapure water. The weight ratio of the dry components in the slurry was 75 wt% of the active material, 20 wt% of conductive carbon, and 5 wt% of CMC. The dispersion was homogenized using a planetary ball-mill. The thus obtained slurry was cast on dendritic Cu foil (Cu $\geq 99.9\%$; Schlenk) using a laboratory-scale doctor blade with a wet film thickness of 140 μm . Disc-shaped electrodes with a diameter of 12 mm were cut and dried at 120 °C under vacuum overnight. The separator and electrolyte were the same as in the previous paragraph and lithium metal foil served as counter electrode. The cell assembly was conducted in an argon-filled glove box. Before the actual experiment an internal calibration of the calorimeter was conducted using a dummy coin cell with a defined resistance. The galvanostatic cycling of the coin cells was performed within a potential range from 3.0 to 0.01 V versus the lithium counter electrode using a BioLogic VSP. The uncertainty of the measurements was less than ± 300 nW.

Polarization and Entropy Analysis: According to the method described by Huie et al.,^[50] the overpotential η and the entropic heat coefficient (dE_{OCV}/dT) were determined from the voltage relaxation of the GITT experiments. For this, the coin cells were placed inside an incubator (BD 23; Binder) at a constant temperature of 20 °C. The cells were allowed to rest for 48 h at OCV before it was dis-/charged at a constant specific current of 50 mA g^{-1} for 60 min. At the end of the current pulse, the cell voltage E_{load} was measured. After 40 h of relaxation, the cell voltage was measured again to determine E_{OCV} . Subsequently, the polarization was estimated from the difference between E_{OCV} and E_{load} . After each relaxation step, the temperature was ramped stepwise from the initial temperature of 20 °C to 10 °C, 20 °C, 30 °C, and back to 20 °C. Each temperature step was held constant for 2 h to allow the OCV to relax. Afterward, the entropic heat coefficient dE_{OCV}/dT was determined by the changes of the OCV values with respect to the temperature intervals. This procedure was repeated at different SODs and SOC to determine the polarization and entropic heat contributions as a function of the SOD or SOC.

Electrochemical Half-Cell Microcalorimetry (HCMC): The microcalorimetric half-cell measurements were conducted in a home-built microcalorimeter,^[40,51,52] attached to a glove box under an argon atmosphere ($\text{O}_2 < 5$ ppm; $\text{H}_2\text{O} < 5$ ppm). As the working electrode (geometrical area of 0.2 cm^2) a dendritic Cu foil was used, coated with the active material, as described above. On top of the working electrode, a propylene electrochemical cell was mounted, sealed with a Viton O-Ring. Li bands (approximately $15 \times 2 \times 1$ mm³) were used as reference and counter electrodes. The cell contained about 500 μL of electrolyte (1 M LiPF_6 in a 1:1 mixture of EC and DMC; UBE). For determining the heat flux during the electrochemically driven processes from the temperature transients, these were deconvoluted by employing the thermal response function of the electrode-sensor assembly, measured by illumination with a 2 ms laser pulse.^[51,52] As discussed above, significant potential relaxation proceeds up to about 100 ms after the pulse. Thus, to include the reversible heat exchange during the relaxation processes, the heat flux was integrated up to 100 ms. To obtain absolute values for the reversible molar heat, the calorimeter was calibrated by measuring the electron transfer reaction in 0.5 M $\text{K}_3[\text{Fe}(\text{CN})_6]/0.5$ M $\text{K}_4[\text{Fe}(\text{CN})_6]$, for which the corresponding molar heat is known from literature.^[51–53] The data points in Figure 6 were obtained as the average from a total of 50 single temperature transient measurements at 10 different potential pulse amplitudes ranging from -300 to $+300$ mV. The absolute errors of the molar heat values were estimated to about 5 kJ mol^{-1} , mainly due to uncertainties from heat evolution of the rather strong background processes. The relative errors for the data points in Figure 6 are much smaller, as can be inferred from their rather smooth course. The reversible molar heat is referenced to the moles of elementary charges, which flowed in the outer cell circuit. It is given for the cathodic direction of the electrochemical processes, i.e., for the discharge (lithiation) process.

From the reversible molar heat, the reaction entropy of the investigated electrochemically driven processes can be directly derived. In principle, since the reversible molar heat of a half-cell reaction was considered,

entropic contributions from the ion transport in solution had to be included.^[40–42] However, due to the expected small entropy of transport of Li⁺ and PF₆⁻ in the organic carbonate-based electrolyte, such contributions were neglected here and the reaction entropy of the half cell process was obtained by dividing the reversible molar heat by the room temperature (300 K; see also the discussion^[44] and the references cited therein). The corresponding reaction entropy scale is plotted at the right axis in Figure 6. The reaction entropy is also given for the cathodic process direction.

Supporting Information

Supporting Information is available from the Wiley Online Library or from the author.

Acknowledgements

J.A. and A.-L.W. contributed equally to this work. Financial support from the Vector Foundation within the NEW E² project and the Helmholtz Association is kindly acknowledged. Moreover, the authors would like to acknowledge the Elettra Sincrotrone Trieste, Italy, for granting beamtime to perform the XAS experiments reported herein (proposal no. 20200299) and Dr. Danilo Oliveira Souza for his support as local contact during the measurements. The research leading to this result had been supported by the project CALIPSOplus under Grant Agreement 730872 from the EU Framework Programme for Research and Innovation HORIZON 2020. M.L. and R.S. gratefully acknowledge funding by the German Research Foundation (DFG) under Project ID 390874152 (POLiS Cluster of Excellence).

Open access funding enabled and organized by Projekt DEAL.

Conflict of Interest

The authors declare no conflict of interest.

Data Availability Statement

The data that support the findings of this study are available from the corresponding author upon reasonable request.

Keywords

alloying, anodes, conversion, lithium batteries, tin oxide

Received: March 3, 2022

Revised: May 6, 2022

Published online:

- [1] M. Marinaro, D. Bresser, E. Beyer, P. Faguy, K. Hosoi, H. Li, J. Sakovica, K. Amine, M. Wohlfahrt-Mehrens, S. Passerini, *J. Power Sources* **2020**, 459, 228073.
- [2] M. Armand, P. Axmann, D. Bresser, M. Copley, K. Edström, C. Ekberg, D. Guyomard, B. Lestriez, P. Novák, M. Petranikova, W. Porcher, S. Trabesinger, M. Wohlfahrt-Mehrens, H. Zhang, *J. Power Sources* **2020**, 479, 228708.
- [3] R. Mukherjee, R. Krishnan, T.-M. Lu, N. Koratkar, *Nano Energy* **2012**, 1, 518.
- [4] M. Li, J. Lu, Z. Chen, K. Amine, *Adv. Mater.* **2018**, 30, 1800561.
- [5] J. Asenbauer, T. Eisenmann, M. Kuenzel, A. Kazzazi, Z. Chen, D. Bresser, *Sustainable Energy Fuels* **2020**, 4, 5387.

- [6] H. Zhang, Y. Yang, H. Xu, L. Wang, X. Lu, X. He, *InfoMat* **2022**, 4, e12228.
- [7] G. Xu, P. Han, S. Dong, H. Liu, G. Cui, L. Chen, *Coord. Chem. Rev.* **2017**, 343, 139.
- [8] O. Riedel, A. Düttmann, S. Dühnen, J. Kolny-Olesiak, C. Gutsche, J. Parisi, M. Winter, M. Knipper, T. Placke, *ACS Appl. Nano Mater.* **2019**, 2, 3577.
- [9] B. Wang, J. Ryu, S. Choi, X. Zhang, D. Pribat, X. Li, L. Zhi, S. Park, R. S. Ruoff, *ACS Nano* **2019**, 13, 2307.
- [10] G. A. Elia, J. Wang, D. Bresser, J. Li, B. Scrosati, S. Passerini, J. Hassoun, *ACS Appl. Mater. Interfaces* **2014**, 6, 12956.
- [11] Y. Lu, L. Yu, X. W. (David) Lou, D. Lou, *Chem* **2018**, 4, 972.
- [12] Y. Jiang, D. Zhang, Y. Li, T. Yuan, N. Bahlawane, C. Liang, W. Sun, Y. Lu, M. Yan, *Nano Energy* **2014**, 4, 23.
- [13] D. Bresser, E. Paillard, P. Niehoff, S. Krueger, F. Mueller, M. Winter, S. Passerini, *ChemPhysChem* **2014**, 15, 2177.
- [14] D. Bresser, S. Passerini, B. Scrosati, *Energy Environ. Sci.* **2016**, 9, 3348.
- [15] Y. Liu, C. Hu, L. Chen, Y. Hu, H. Jiang, C. Li, *J. Energy Chem.* **2022**, 69, 450.
- [16] C. Hu, L. Chen, Y. Hu, A. Chen, L. Chen, H. Jiang, C. Li, *Small* **2021**, 17, 2103532.
- [17] J. Wang, L. Wang, S. Zhang, S. Liang, X. Liang, H. Huang, W. Zhou, J. Guo, *J. Alloys Compd.* **2018**, 748, 1013.
- [18] M. Lübke, D. Ning, C. F. Armer, D. Howard, D. J. L. Brett, Z. Liu, J. A. Darr, *Electrochim. Acta* **2017**, 242, 400.
- [19] A. Birrozzi, J. Asenbauer, T. E. Ashton, A. R. Groves, D. Geiger, U. Kaiser, J. A. Darr, D. Bresser, *Batteries Supercaps* **2020**, 3, 284.
- [20] F. Mueller, D. Bresser, V. S. K. Chakravadhanula, S. Passerini, *J. Power Sources* **2015**, 299, 398.
- [21] Y. Ma, Y. Ma, G. Giuli, T. Diemant, R. J. Behm, D. Geiger, U. Kaiser, U. Ulissi, S. Passerini, D. Bresser, *Sustainable Energy Fuels* **2018**, 2, 2601.
- [22] Y. Ma, Y. Ma, U. Ulissi, Y. Ji, C. Streb, D. Bresser, S. Passerini, *Electrochim. Acta* **2018**, 277, 100.
- [23] J. Asenbauer, A. Varzi, S. Passerini, D. Bresser, *J. Power Sources* **2020**, 473, 228583.
- [24] K. Govaerts, B. Partoens, D. Lamoen, *Solid State Commun.* **2016**, 243, 36.
- [25] “Crystallography Open Database”, <http://www.crystallography.net/cod/9007433.html> (accessed: February 2022).
- [26] M. Fracchia, P. Ghigna, A. Minguzzi, A. Vertova, F. Turco, G. Cerrato, D. Meroni, *Nanomaterials* **2020**, 10, 1224.
- [27] N. S. Garnet, V. Ghodsi, L. N. Hutflus, P. Yin, M. Hegde, P. V. Radovanovic, *J. Phys. Chem. C* **2017**, 121, 1918.
- [28] G. Giuli, A. Trapananti, F. Mueller, D. Bresser, F. D’Acapito, S. Passerini, *Inorg. Chem.* **2015**, 54, 9393.
- [29] T. Eisenmann, A. Birrozzi, A. Mullaliu, G. Giuli, A. Trapananti, S. Passerini, D. Bresser, *J. Electrochem. Soc.* **2021**, 168, 030503.
- [30] S. Indris, M. Scheuermann, S. M. Becker, V. Šepelák, R. Kruk, J. Suffner, F. Gyger, C. Feldmann, A. S. Ulrich, H. Hahn, *J. Phys. Chem. C* **2011**, 115, 6433.
- [31] I. Sandu, T. Brousse, D. M. Schleich, M. Danot, *J. Solid State Chem.* **2004**, 177, 4332.
- [32] J. Chouvin, J. Olivier-Fourcade, J. C. Jumas, B. Simon, P. Biensan, F. J. F. Madrigal, J. L. Tirado, C. P. Vicente, *J. Electroanal. Chem.* **2000**, 494, 136.
- [33] P. Möller, P. Dulski, W. Szacki, G. Malow, E. Riedel, *Geochim. Cosmochim. Acta* **1988**, 52, 1497.
- [34] J. Sakuma, K. Nomura, C. Barrero, M. Takeda, *Thin Solid Films* **2007**, 515, 8653.
- [35] U. G. Nwokeke, R. Alcántara, J. L. Tirado, R. Stoyanova, M. Yoncheva, E. Zhecheva, *Chem. Mater.* **2010**, 22, 2268.
- [36] J. Asenbauer, A. Hoefling, S. Indris, J. Tübke, S. Passerini, D. Bresser, *ACS Appl. Mater. Interfaces* **2020**, 12, 8206.
- [37] A. Trapananti, T. Eisenmann, G. Giuli, F. Mueller, A. Moretti, S. Passerini, D. Bresser, *Mater. Today Chem.* **2021**, 20, 100478.

- [38] K. Furuya, K. Ogawa, Y. Mineo, A. Matsufuji, J. Okuda, T. Erata, *J. Phys.: Condens. Matter* **2001**, *13*, 3519.
- [39] T. Eisenmann, J. Asenbauer, S. J. Rezvani, T. Diemant, R. J. Behm, D. Geiger, U. Kaiser, S. Passerini, D. Bresser, *Small Methods* **2021**, *5*, 2001021.
- [40] R. Schuster, *Curr. Opin. Electrochem.* **2017**, *1*, 88.
- [41] T. Ozeki, I. Watanabe, S. Ikeda, *J. Electroanal. Chem. Interfacial Electrochem.* **1983**, *152*, 41.
- [42] J. N. Agar, *Advances in Electrochemistry and Electrochemical Engineering*, Vol. 3, Wiley, New York **1963**.
- [43] M. J. Schmid, J. Xu, J. Lindner, P. Novák, R. Schuster, *J. Phys. Chem. B* **2015**, *119*, 13385.
- [44] M. J. Schmid, K. R. Bickel, P. Novák, R. Schuster, *Angew. Chem., Int. Ed.* **2013**, *52*, 13233.
- [45] L. E. Downie, S. R. Hyatt, J. R. Dahn, *J. Electrochem. Soc.* **2016**, *163*, A35.
- [46] S. J. Rezvani, R. Gunnella, A. Witkowska, F. Mueller, M. Pasqualini, F. Nobili, S. Passerini, A. Di Cicco, *ACS Appl. Mater. Interfaces* **2017**, *9*, 4570.
- [47] Y. Joly, *Phys. Rev. B* **2001**, *63*, 125120.
- [48] L. Hedin, B. I. Lundqvist, S. Lundqvist, *Solid State Commun.* **1971**, *9*, 537.
- [49] D. Bresser, E. Paillard, R. Kloepsch, S. Krueger, M. Fiedler, R. Schmitz, D. Baither, M. Winter, S. Passerini, *Adv. Energy Mater.* **2013**, *3*, 513.
- [50] M. M. Huie, D. C. Bock, L. Wang, A. C. Marschilok, K. J. Takeuchi, E. S. Takeuchi, *J. Phys. Chem. C* **2018**, *122*, 10316.
- [51] S. Frittmann, V. Halka, C. Jaramillo, R. Schuster, *Rev. Sci. Instrum.* **2015**, *86*, 064102.
- [52] K. R. Bickel, K. D. Etzel, V. Halka, R. Schuster, *Electrochim. Acta* **2013**, *112*, 801.
- [53] P. Boudeville, *Inorg. Chim. Acta* **1994**, *226*, 69.